arXiv:2105.05562v1 [cond-mat.mtrl-sci] 12 May 2021

Procedure for 3D atomic resolution reconstructions using atom-counting and a Bayesian genetic algorithm

Annick De Backer,[1,2] Sandra Van Aert,[1,2,*] Peter D. Nellist,[3] and Lewys Jones[4,5,†]

[1] *EMAT, University of Antwerp, Groenenborgerlaan 171, 2020 Antwerp, Belgium*
[2] *NANOlab Center of Excellence, University of Antwerp, Groenenborgerlaan 171, 2020 Antwerp, Belgium*
[3] *Department of Materials, University of Oxford, Parks Road, OX1 3PH Oxford, United Kingdom*
[4] *Advanced Microscopy Laboratory, Centre for Research on Adaptive Nanostructures and Nanodevices (CRANN), Dublin 2, Ireland*
[5] *School of Physics, Trinity College Dublin, The University of Dublin, Dublin 2, Ireland*

(Dated: May 13, 2021)

We introduce a Bayesian genetic algorithm for reconstructing atomic models of nanoparticles from a single projection using Z-contrast imaging. The number of atoms in a projected atomic column obtained from annular dark field scanning transmission electron microscopy (ADF STEM) images serves as an input for the initial three-dimensional (3D) model. The novel algorithm minimizes the energy of the structure while utilising *a priori* information about the finite precision of the atom-counting results and neighbor-mass relations. The results show excellent prospects for obtaining reliable reconstructions of beam-sensitive nanoparticles during dynamical processes from images acquired with sufficiently low incident electron doses.

It is commonly accepted that the three-dimensional (3D) atomic structure of metallic nanoparticles determines their catalytic properties [1–5]. Indeed, the presence of highly undercoordinated atoms or stepped facets at the surface govern many catalytic reactions. A quantitative characterization of the atomic configuration at the surface of these metallic nanoparticles is therefore essential to reveal the active sites of the nanoparticle where reactant molecules are preferentially adsorbed, to understand the mechanisms of the catalytic behavior, and to improve the performance of these systems. Atomic resolution annular dark field scanning transmission electron microscopy (ADF STEM) has become an invaluable tool for imaging metallic nanostructures [6–10]. In this context, electron tomography has been used to provide insights in the 3D shape of nanostructures [11–13], but this technique requires a significant electron dose for the multiple projections. Consequently, this approach is not feasible when investigating small beam-sensitive catalysts or dynamical processes. Therefore, an alternative method has been developed where the 3D atomic structure is reconstructed from a single ADF STEM projection image [8, 14, 15]. For this purpose, the number of atoms contained in an atomic column along the third dimension is retrieved from an ADF STEM image. These atom counts are used to create an initial atomic model which serves as an input for an energy minimization to obtain a relaxed 3D reconstruction of a nanostructure. The validity of this atom-counting/energy minimization method has qualitatively been verified using electron tomography and is applied to study several systems [10, 15].

Two possible approaches for the energy minimization are nowadays available. Using the first approach, the energy is minimized by shifting the atomic columns up and down while keeping the number of atoms in a column fixed to the outcome of the atom-counting procedure [8, 16]. The second approach consists of a full molecular dynamics simulation to relax the particle's structure [5, 10, 15]. The first method is potentially too restrictive by ignoring the finite atom-counting precision, especially at lower doses. The expected inevitable counting imprecision in this case [9], will likely result in slightly more roughness at the reconstructed atomic surface in the direction parallel to the beam direction [8, 15]. On the other hand, the second method runs the risk of ending up in a global energy minimum and violating the physical constraints of the experimental observation. Both approaches hamper a reliable 3D reconstruction of the atomic configuration at the surface, especially

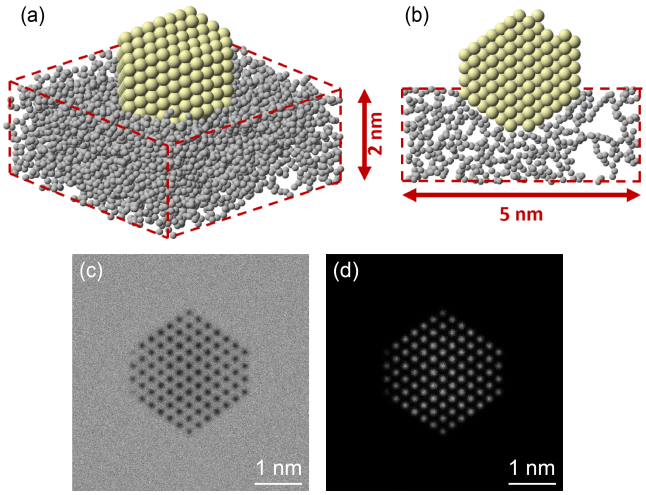

Figure 1. (a) 3D model and (b) cross-section of the Pt nanoparticle model partially embedded in an amorphous carbon support, (c) simulated ABF STEM image and (d) simulated ADF STEM image at 10^4 $e^-/Å^2$.

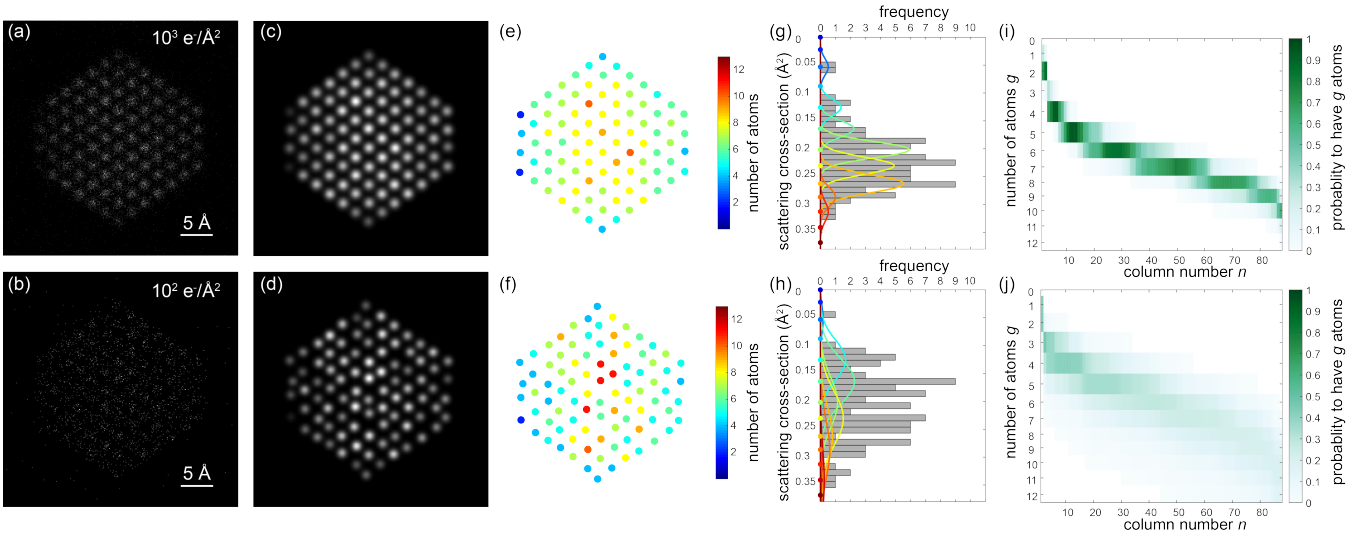

Figure 2. (a-b) Simulated ADF STEM images of the Pt nanoparticle embedded in the carbon support along the [110] zone axis for an incident electron dose of 10^3 e$^-$/Å^2 and 10^2 e$^-$/Å^2. (c-d) Refined parametric models of the images shown in (a-b). (e-f) Estimated number of atoms in each atomic column for the images shown in (a-b). (g-h) Histograms of SCSs for the images shown in (a-b). The decomposition into overlapping Gaussian components is shown in color, corresponding to the number of atoms. (i-j) Probability matrices indicating the probability for a column n to contain a specific number of atoms g.

for images acquired at lower doses. Here we propose a new method which includes the finite atom-counting precision via a Bayesian inference scheme to improve the 3D atomic models for small nanostructures. Moreover, the incorporation of additional prior knowledge from neighbor-mass relations will be beneficial when reconstructing atomic models from extremely low dose ADF STEM images. This prior knowledge is fused into a genetic algorithm which uses atom-counting results as an input for reconstructing the 3D atomic structure. In this Letter, we introduce this advanced Bayesian genetic algorithm and evaluate quantitatively via an extensive simulation study the quality of the obtained reconstructions in terms of the reliability with which the surface atoms can be reconstructed in 3D. In the last part, the algorithm is applied to retrieve 3D atomic models from an experimental time-series of a Pt nanoparticle.

To count the number of atoms, so-called scattering cross sections (SCSs), corresponding to the total intensity of electrons scattered toward the ADF detector for every atomic column, have been introduced in ADF STEM. These SCSs can be measured using statistical parameter estimation theory [17, 18] or by integrating intensities over the probe positions in the vicinity of a single column of atoms [19]. For our simulation study, SCSs are determined from noise realizations at different doses of a simulated ADF STEM image of a Pt nanoparticle partially embedded in a carbon support, illustrated in Fig. 1(a-b). The created particle largely resembles the Wulff construction solid for Pt_{586} (4 atoms along each edge) and was modified to include several diagnostic features of interest commonly observed for catalytic metallic nanoparticles including a surface adatom, a surface vacancy, a terrace edge, a small area of {110} face, and rounded corners. With these modifications the particle model contains 587 atoms. The slab of amorphous carbon measures 5 nm × 5 nm × 2 nm and the geometry follows the work of reference [20]. Image simulations were performed for the Pt particle viewed along the [110] zone axis using the MULTEM package [21, 22]. An acceleration voltage of 200 kV, a semi-convergence angle of 22.48 mrad, and a pixel size of 0.124 Å were chosen and averaging over 30 unique phonon configurations was performed. A source size having a FWHM of 1.0 Å was added to further reflect experiments recorded under the same conditions. Fig. 1(c) shows the annular bright field (ABF) STEM image with a detector collection range of 9-21 mrad, illustrating the presence of the carbon support and Fig. 1(d) shows the ADF STEM image with a detector collection range of 52-248 mrad, using an electron dose of 10^4 e$^-$/Å^2. In Figs. 2(a-b) simulated ADF STEM images are shown using lower incident electron doses with respective 10^3 e$^-$/Å^2 and 10^2 e$^-$/Å^2. The simulated ADF STEM images can be modeled as a superposition of Gaussian functions using the StatSTEM software [15]. The refined models for the simulated ADF STEM images are shown in Figs. 2(c-d). From the estimated model parameters, the SCSs are determined for each atomic column and can be represented in a histogram in Figs. 2(g-h). In a subsequent analysis, the distribution of the SCSs of all atomic columns is decomposed into overlapping normal distributions, i.e. a Gaussian mixture model, as illustrated in Figs. 2(g-h) [23, 24].

The locations of the normal distributions are matched to the expected SCS values for a column containing g atoms [25] and their widths are determined (details can be found in the Supplementary Material). The number of atoms in each projected atomic column in Figs. 2(e-f) is then obtained by assigning the SCS to the component that generates this SCS value with the highest probability. The width of the normal distributions reflects the finite precision of the atom-counting results, which will be used as prior knowledge in the genetic algorithm for reconstructing the 3D atomic structure. As an input we need the probability that an atomic column contains a specific number of atoms and this can be defined from the decomposition into normal distributions, illustrated in Figs. 2(g-h). Indeed, the normal distribution functions describe the probability that component g generates the nth SCS, i.e. $p(SCS_n|g)$, and by using Bayes' theorem, the probability that the nth SCS has g atoms can be computed $p(g|SCS_n)$:

$$p(g|SCS_n) = \frac{p(g)p(SCS_n|g)}{p(SCS_n)} = \frac{p(g)p(SCS_n|g)}{\sum_g p(g)p(SCS_n|g)}. \tag{1}$$

Equal probabilities are assigned to the probability for having g atoms in a column $p(g)$. $p(g|SCS_n)$ is visualized by a probability matrix in Figs. 2(i-j). From the representation of the Gaussian mixture model on top of the histogram, the relation between the probability matrix and the width of the normal distributions is clearly illustrated.

For improving the quality of the low-dose reconstructions, we can include even more relevant prior knowledge. For spherical convex nanoparticles, we can include neighbor-mass relations because abrupt discontinuities are highly non-physical for small nanoparticles [26]. The neighbor-mass matrix helps to predict the column mass based on the average mass of the neighboring columns. For small nanoparticles, we propose a diagonal neighbor-mass matrix. The matrix is visualized in Fig. S1 of the Supplementary Material. The probability profile is Gaussian and the width of this Gaussian is chosen such that the interval ±1 and ±0 atoms contains 80% of the probability. The normalized neighbor-mass probability, $p(g|NB_n)$ with NB_n indicating the average neighbor-mass, is combined with the probability matrix accounting for the atom-counting reliability $p(g|SCS_n)$, in order to take the two types of prior knowledge into account:

$$p\left(g|\text{column}_n\right) = \frac{p(g|SCS_n)p(g|NB_n)}{\sum_g p(g|SCS_n)p(g|NB_n)}. \tag{2}$$

This final probability matrix is used as input of the prior knowledge for the genetic algorithm that we will use to reconstruct the 3D atomic structure of the nanoparticle, hence the name Bayesian genetic algorithm. Genetic algorithms are powerful tools for solving large optimization problems where finding a direct solution is not possible [27–31]. It is an iterative process where first a population of randomly generated individuals is created. In our algorithm, this initial population is generated by randomly modifying the number of atoms and the height offset of the atomic columns of a 3D starting configuration within a certain mutation range. This 3D starting configuration is obtained by positioning the atoms (i.e. the outcome of the atom-counting procedure) in each atomic column parallel to the beam direction and symmetrically around a central plane. A population size of 500 is used in all calculations, the count mutation range equals 1, and the height mutation range for the offset of a column equals a lattice step. In each iteration, i.e. a generation, the fitness of every individual in the population is evaluated by the cost-function of the optimization problem. The individuals with the best cost-function values are selected from the current population, and a new complete population of candidate solutions is formed by recombining and mutating the selected individuals. The fraction of the population that is used for the recombination step equals 50%. For each recombined member, two parents are randomly chosen from the selected individuals, and cross-over is performed by randomly selecting columns from both parents. A mutation density of 2% is included to avoid ending up immediately in a local minimum by randomly modifying the number of atoms and height offset for 2% of the atomic columns in each new member. In addition to the usual iterations over many breeding generations, in this work we introduce a second loop to provide for multiple unique starting initializations, specifically to reduce the risk of finding only local-minima solutions. The cost-function χ that we use here to evaluate the candidate solutions is given by:

$$\chi = \frac{\sum E_a}{\sum_n g_n} \cdot \sqrt[n]{\prod_n p(g|\text{column}_n)}, \tag{3}$$

where $\sum E_a$ is the sum of the energies per atom given by the EAM potential [32, 33], $\sum_n g_n$ is the total particle mass. This cost-function consists of two factors where the first represents the average energy per atom which we wish to minimize. The second factor represents the probability of the candidate solution based on the introduced prior knowledge (Eq.(2)). This factor itself is based on the geometric mean of the probabilities of each individual column and needs to be maximized. Since the average energy per atom is negative, this cost-function is minimized in order to reconstruct the 3D model.

In order to evaluate the quality of the reconstructions using the Bayesian genetic algorithm, an extensive simulation study is carried out. For this purpose, the electron dose is varied between 10^2 $e^-/Å^2$ and 10^5 $e^-/Å^2$ and 30 noise realizations are generated at each electron dose. Fig. S2 in the Supplementary Material summarizes the atom-counting results obtained following the methodol-

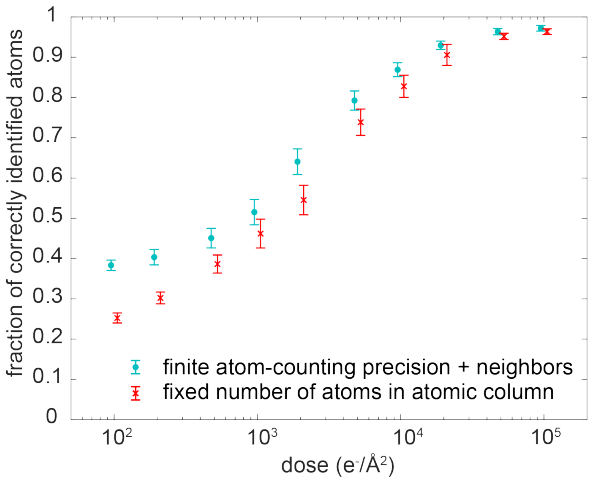

Figure 3. Fraction of the surface atoms with the same coordination number as in the ground truth model with 95% error bars when including the finite atom-counting precision and neighbor-mass relations as prior knowledge. As a reference, the results when using a fixed number of atoms in a column are also displayed.

ogy illustrated in Fig. 2 and which are used as an input for our Bayesian genetic algorithm. For each reconstruction, 25 unique random starting initialization structures are used in the algorithm. It should be noted that a structure with a better cost-function might be found when increasing this number. The results of the reconstructions are quantitatively summarized by comparing the reconstructed 3D models with the ground truth model. As a criterion to evaluate the 3D atomic models, we used the fraction of surface atom positions, i.e. with coordination number less than 12, that are correctly defined in 3D and that have the same coordination number as in the ground truth model. These are the atoms which are of interest for catalysis. The coordination number serves as a powerful predictor for surface adsorption strength on Pt nanoparticles, and hence as a predictor of chemical activity [3, 34–36]. Fig. 3 shows this fraction for the reconstructed atomic models. As a reference, we also included the fraction following the approach where the number of atoms is fixed to the outcome of the atom-counting procedure and where during the reconstruction the atomic columns are only shifted up and down. A significant, vast improvement for the reconstructed surface atoms is observed when including the finite atom-counting precision and the neighbor-mass relations, especially for the lower incident electron doses.

In order to evaluate the reconstructed 3D atomic models in a bit more detail, the 4th worst and 4th best reconstructions of the 30 noise realizations at each dose can be visualized as a kind of a 80% confidence interval of the reconstructions. These intervals are shown in Fig. 4. The colors of the atoms correspond to the coordination number of the atoms. Even for the lower doses, the shape is very well reconstructed and a vast improvement is observed when including relevant prior knowledge resulting in less roughness from the finite atom-counting precision at the surface.

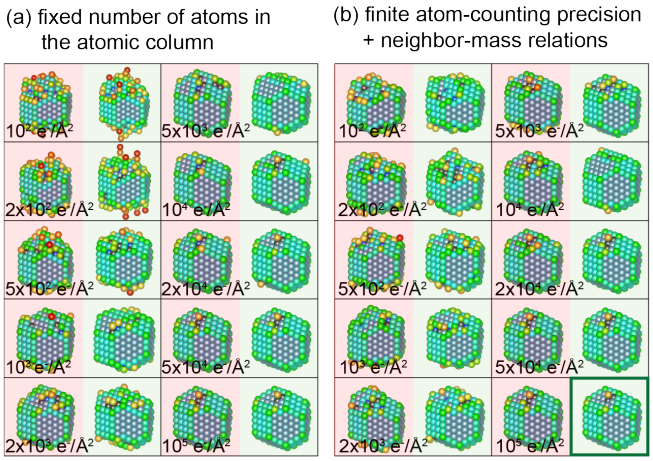

Figure 4. Visualization of the reconstructed 3D atomic models represented by the lower bound (red background) and upper bound (green background) of a 80% confidence interval for the reconstructions when using (a) a fixed number of atoms in the atomic column during the reconstruction and (b) the finite atom-counting precision and the neighbor-mass relations. The reconstruction in the box corresponds to the ground truth model.

As a last part in this Letter, we apply the Bayesian genetic algorithm to 25 frames of an experimental time series of a catalyst Pt nanoparticle [26]. The experimental details and corrections for scan noise and tilt are described in the Supplementary Material. To reliably count the number of atoms from the time series of images, we used a hidden Markov model which explicitly describes the possibility of structural changes over time [37, 38]. The atom-counting results from each single frame have been used as an input for our Bayesian genetic algorithm in which we employ the finite atom-counting precision and neighbor-mass relations. For the experimental time series, we used 100 unique initializations throughout the reconstruction procedure. The reconstructed models are schematically represented in Fig. 5. The ADF STEM images and corresponding reconstructed models for all frames are shown in Supporting Figs. S3 and S4. This approach enables a reliable 3D quantification of the structural changes of the Pt nanoparticle under the electron beam. From the evaluation of the coordination numbers (Fig. S5 of the Supplementary Material), we can conclude that although each image has unique noise and that the structure is moving under the electron beam, the number of atoms with the same coordination number is consistent throughout time. Since these coordination numbers are very important to relate to the catalytic properties,

it is important to point out here that the small changes clearly do not change the overall catalysis-relevant information that we can extract.

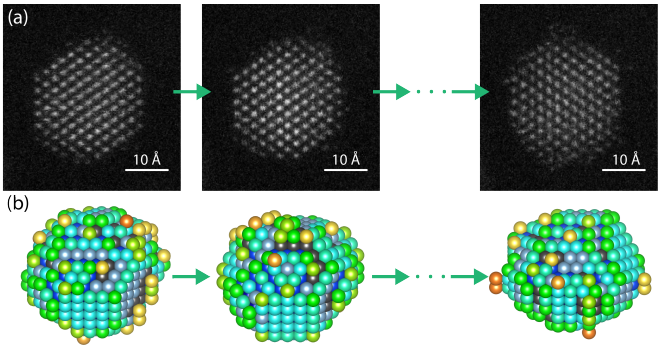

Figure 5. (a) Experimental ADF STEM time series of a Pt nanoparticle. (b) Reconstructed atomic models for the time sequence.

To summarize and conclude, we introduced a powerful alternative to the initially developed atom-counting/energy minimization method for the 3D reconstruction of nanoparticles from a single viewing projection. This newly designed Bayesian genetic algorithm takes advantage of the finite atom-counting precision and neighbor-mass relations during the reconstruction. This results in more reliable reconstructions of the 3D atomic structure, especially at lower incident electron doses below 10^4 $e^-/\text{Å}^2$. The increased quality of the 3D atomic models has been validated by a quantitative evaluation of the coordination numbers of the surface atoms. This result shows great promise to use these reconstructions to predict the adsorption properties of catalytic nanoparticles.

This work was supported by the European Research Council (Grant 770887 PICOMETRICS to SVA and Grant 823717 ESTEEM3). The authors acknowledge financial support from the Research Foundation Flanders (FWO, Belgium) through project fundings and a postdoctoral grant to ADB. LJ acknowledges Science Foundation Ireland (SFI - grant number URF/RI/191637), the Royal Society, and the AMBER Centre. The authors acknowledge Aakash Varambhia for his assistance and expertise with the experimental recording and use of characterization facilities within the David Cockayne Centre for Electron Microscopy, Department of Materials, University of Oxford and in particular the EPSRC (EP/K040375/1 South of England Analytical Electron Microscope)

* sandra.vanaert@uantwerpen.be
† lewys.jones@tcd.ie

[1] R. Narayanan and M. A. El-Sayed, Nano Letters **4**, 1343 (2004).
[2] F. Tao, S. Dag, L.-W. Wang, Z. Liu, D. R. Butcher, H. Bluhm, M. Salmeron, and G. A. Somorjai, Science **327**, 850 (2010).
[3] F. Calle-Vallejo, P. Sautet, and D. Loffreda, The Journal of Physical Chemistry Letters **5**, 3120 (2014).
[4] H. Barron and A. S. Barnard, Catalysis Science & Technology **5**, 2848 (2015).
[5] P. Liu, E. Arslan Irmak, A. De Backer, A. De wael, I. Lobato, A. Béché, S. Van Aert, and S. Bals, Nanoscale **13**, 1770 (2021).
[6] T. Fujita, P. Guan, K. McKenna, X. Lang, A. Hirata, L. Zhang, T. Tokunaga, Y. Arai, N. Tanaka, Y. Ishikawa, N. Asao, Y. Yamamoto, J. Erlebacher, and M. Chen, Nature Materials **11**, 775 (2012).
[7] A. B. Yankovich, B. Berkels, W. Dahmen, P. Binev, S. I. Sanchez, S. A. Bradley, A. Li, I. Szlufarska, and Voy, Nature Communications **5**, 4155 (2014).
[8] L. Jones, K. E. MacArthur, V. T. Fauske, A. T. J. van Helvoort, and P. D. Nellist, Nano Letters **14**, 6336 (2014).
[9] A. De Backer, G. T. Martinez, K. E. MacArthur, L. Jones, A. Béché, P. D. Nellist, and S. Van Aert, Ultramicroscopy **151**, 56 (2015).
[10] T. Altantzis, I. Lobato, A. De Backer, A. Béché, Y. Zhang, S. Basak, M. Porcu, Q. Xu, A. Saánchez-Iglesias, L. M. Liz-Marzán, G. Van Tendeloo, S. Van Aert, and S. Bals, Nano Letters **19**, 477 (2019).
[11] S. Van Aert, K. J. Batenburg, M. D. Rossell, R. Erni, and G. Van Tendeloo, Nature **470**, 374 (2011).
[12] S. Bals, B. Goris, L. M. Liz-Marzán, and G. Van Tendeloo, Angewandte Chemie **53**, 10600 (2014).
[13] J. Miao, P. Ercius, and J. L. Billinge, Science **353**, 1380 (2016).
[14] S. Bals, S. Van Aert, C. P. Romero, K. Lauwaet, M. J. Van Bael, B. Schoeters, B. Partoens, E. Yücelen, P. Lievens, and G. Van Tendeloo, Nature Communications **3**, 897 (2012).
[15] A. De Backer, L. Jones, I. Lobato, T. Altantzis, B. Goris, P. D. Nellist, S. Bals, and S. Van Aert, Nanoscale **9**, 8791 (2017).
[16] J. J. Geuchies, C. van Overbeek, W. H. Evers, B. Goris, A. De Backer, G. P. Gantapara, F. T. Rabouw, J. Hilhorst, J. L. Peters, O. Konovalov, A. V. Petukhov, M. Dijkstra, L. D. A. Siebbeles, S. Van Aert, S. Bals, and D. Vanmaekelbergh, Nature Materials **15**, 1248 (2016).
[17] S. Van Aert, J. Verbeeck, R. Erni, S. Bals, M. Luysberg, D. Van Dyck, and G. Van Tendeloo, Ultramicroscopy **109**, 1236 (2009).
[18] A. De Backer, K. H. W. van den Bos, W. Van den Broek, J. Sijbers, and S. Van Aert, Ultramicroscopy **171**, 104 (2016).
[19] H. E, K. E. MacArthur, T. J. Pennycook, E. Okunishi, A. J. D'Alfonso, N. R. Lugg, L. J. Allen, and P. D. Nellist, Ultramicroscopy **133**, 109 (2013).
[20] C. Ricolleau, Y. Le Bouar, H. Amara, O. Landon-Cardinal, and D. Alloyeau, Journal of Applied Physics **114**, 213504 (2013).
[21] I. Lobato and D. Van Dyck, Ultramicroscopy **156**, 9 (2015).
[22] I. Lobato, S. Van Aert, and J. Verbeeck, Ultramicroscopy **168**, 17 (2016).
[23] A. De Backer, G. T. Martinez, A. Rosenauer, and

S. Van Aert, Ultramicroscopy **134**, 23 (2013).
[24] S. Van Aert, A. De Backer, G. T. Martinez, B. Goris, S. Bals, G. Van Tendeloo, and A. Rosenauer, Physical Review B **87**, 064107 (2013).
[25] A. De wael, A. De Backer, L. Jones, P. D. Nellist, and S. Van Aert, Ultramicroscopy **177**, 69 (2017).
[26] J. Aarons, L. Jones, A. Varambhia, K. E. MacArthur, D. Ozkaya, M. Sarwar, C.-K. Skylaris, and P. D. Nellist, Nano Letters **17**, 4003 (2017).
[27] R. L. Johnston, Dalton Transactions , 4193 (2003).
[28] N. Dugan and S. Erkoç, Algorithms **2**, 410 (2009).
[29] G. Rossi and R. Ferrando, Journal of Physics: Condensed Matter **21**, 084208 (2009).
[30] X. Wu and G. Wu, Chemical Physics **440**, 94 (2014).
[31] M. Yu, A. B. Yankovich, A. Kaczmarowksi, D. Morgan, and P. M. Voyles, ACS Nano **10**, 4031 (2016).
[32] S. M. Foiles, M. I. Baskes, and M. S. Daw, Physical Review B **33**, 7983 (1986).
[33] B.-J. Lee, J.-H. Shim, and M. I. Baskes, Physical Review B **68**, 144112 (2003).
[34] F. Calle-Vallejo, J. I. Martinez, J. M. García-Lastra, P. Sautet, and D. Loffreda, Angewandte Chemie International Edition **53**, 8316 (2014).
[35] F. Calle-Vallejo, D. Loffreda, M. T. Koper, and P. Sautet, Nature Chemistry **7**, 403 (2015).
[36] F. Calle-Vallejo, J. Tymoczko, V. Colic, Q. H. Vu, M. D. Pohl, K. Morgenstern, D. Loffredo, P. Sautet, W. Schuhmann, and A. S. Bandarenka, Science **350**, 185 (2015).
[37] A. De wael, A. De Backer, L. Jones, A. Varambhia, P. D. Nellist, and S. Van Aert, Physical Review Letters **124**, 106105 (2020).
[38] A. De wael, A. De Backer, and S. Van Aert, Ultramicroscopy **219**, 113131 (2020).

arXiv:2105.05562v1 [cond-mat.mtrl-sci] 12 May 2021

Supplementary material
Procedure for 3D atomic resolution reconstruction using atom-counting and a Bayesian genetic algorithm

Annick De Backer,[1] Sandra Van Aert,[1,*] Peter D. Nellist,[2] and Lewys Jones[3,4]

[1] *EMAT, University of Antwerp, Groenenborgerlaan 171, 2020 Antwerp, Belgium*
[2] *Department of Materials, University of Oxford, Parks Road, OX1 3PH Oxford, United Kingdom*
[3] *Advanced Microscopy Laboratory, Centre for Research on Adaptive Nanostructures and Nanodevices (CRANN), Dublin 2, Ireland*
[4] *School of Physics, Trinity College Dublin, The University of Dublin, Dublin 2, Ireland*

EFFECTIVE WIDTH OF THE NORMAL DISTRIBUTIONS IN THE GAUSSIAN MIXTURE MODEL

In principle, the width is estimated from the decomposition into overlapping normal distributions σ_{all} to the set of SCSs values. This width takes into account all uncertainties in the SCSs, including the limited electron dose and fluctuations in the SCSs from other effects such as the carbon support, different vertical onset of columns of the same number of atoms, intensity transfer between columns, and the influence of neighboring columns of different number of atoms [1]. However, it is known that the width of the Gaussian distributions might be underestimated for lower electron doses [2]. Here, we will assess whether the width is underestimated and adjust it when necessary. This will be done by comparing the estimated width σ_{all} with the expected width for the normal distributions from the limited electron dose σ_{dose}. If σ_{dose} is larger than σ_{all}, then this indicates an underestimation from the Gaussian mixture model analysis. The width σ_{dose} can be predicted by [3]:

$$\sigma_{\text{dose}} = \sqrt{\mu_g / d}, \tag{1}$$

where μ_g corresponds to the expected SCS for a column containing g atoms and d equals the incident electron dose. Next, this width σ_{dose} is compared to the width estimated from the decomposition into normal distributions σ_{all}. In order to avoid the underestimation of the width, an effective width is therefore introduced which is the maximum of the two contributions:

$$\sigma_{\text{eff}} = max(\sigma_{\text{dose}}, \sigma_{\text{all}}). \tag{2}$$

σ_{dose} will be dominant when the fluctuations in the SCSs are mainly dose-limited [3].

EXPERIMENTAL PT SERIES

The ADF STEM images were recorded on a JEOL ARM200CF fitted with a probe-aberration corrector using an acceleration voltage of 200 kV, a probe convergence angle of 22.48 mrad, an annular detector ranging from 52-248 mrad, a dwell time of 4 μs and an incident electron dose of $1.38 \cdot 10^4 e^-/\text{Å}^2$ per frame. The images of the time series were corrected for drift and other distortions using non-rigid registration [4]. During the time-series, the Pt nanoparticle tilts slightly away from zone axis orientation and back, which affects the scattering cross-sections [5]. Therefore, the scattering cross-sections of the individual frames need to be compensated for tilt. This is done by using a linear scaling of the scattering cross-sections of the individual frames [2], assuming that the total number of atoms in the nanoparticle remains constant throughout the time series. This assumption is valid since the threshold energy for sputtering Pt atoms from a convex surface with step sites is 379 keV [6], well above the incident electron energy of 200 keV. We therefore do not expect sputtering of atoms from the surface, only surface diffusion [3].

* sandra.vanaert@uantwerpen.be

[1] A. De Backer, G. T. Martinez, A. Rosenauer, and S. Van Aert, Ultramicroscopy **134**, 23 (2013).
[2] A. De wael, A. De Backer, L. Jones, P. D. Nellist, and S. Van Aert, Ultramicroscopy **177**, 69 (2017).
[3] S. Van Aert, A. De Backer, L. Jones, G. T. Martinez, A. Béché, and P. D. Nellist, Physical Review Letters **122**, 066101 (2019).
[4] L. Jones, H. Yang, T. J. Pennycook, S. J. Marshall, S. Van Aert, N. D. Browning, M. R. Castell, and P. D. Nellist, Advanced Structural and Chemical Imaging (2015).
[5] K. E. MacArthur, A. J. D'Alfonso, D. Ozkaya, L. J. Allen, and P. D. Nellist, Ultramicroscopy **156**, 1 (2015).
[6] R. F. Egerton, R. McLeod, F. Wang, and M. Malac, Ultramicroscopy **110**, 991 (2010).

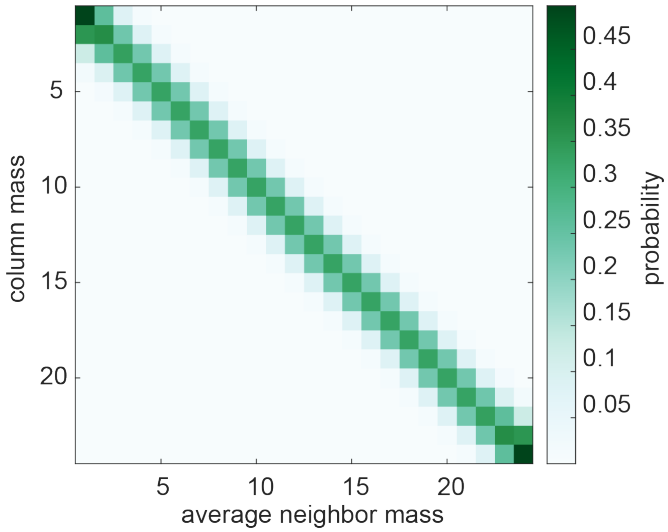

Figure 1. Neighbor-mass probability matrix displaying the average mass of the neighboring columns on the x-axis and the column mass on the y-axis. The colormap illustrates the probabilities.

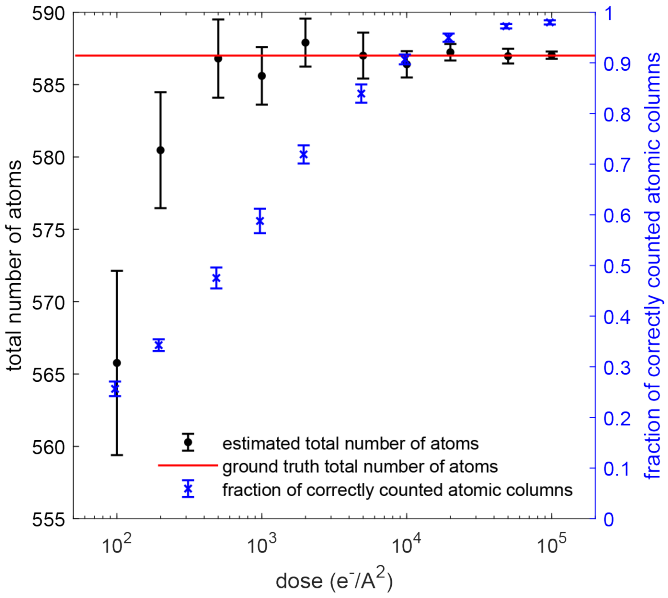

Figure 2. Estimated total number of atoms in the particle (left axis) and the fraction of atomic columns in which the number of atoms has been counted correctly (right blue axis). The error bars indicate 95% confidence intervals. For the lowest doses, the total number of atoms is slightly underestimated and as expected the fraction of correctly counted atomic columns decreases when the incident electron dose decreases. These atom-counting results are used as an input for our Bayesian genetic algorithm.

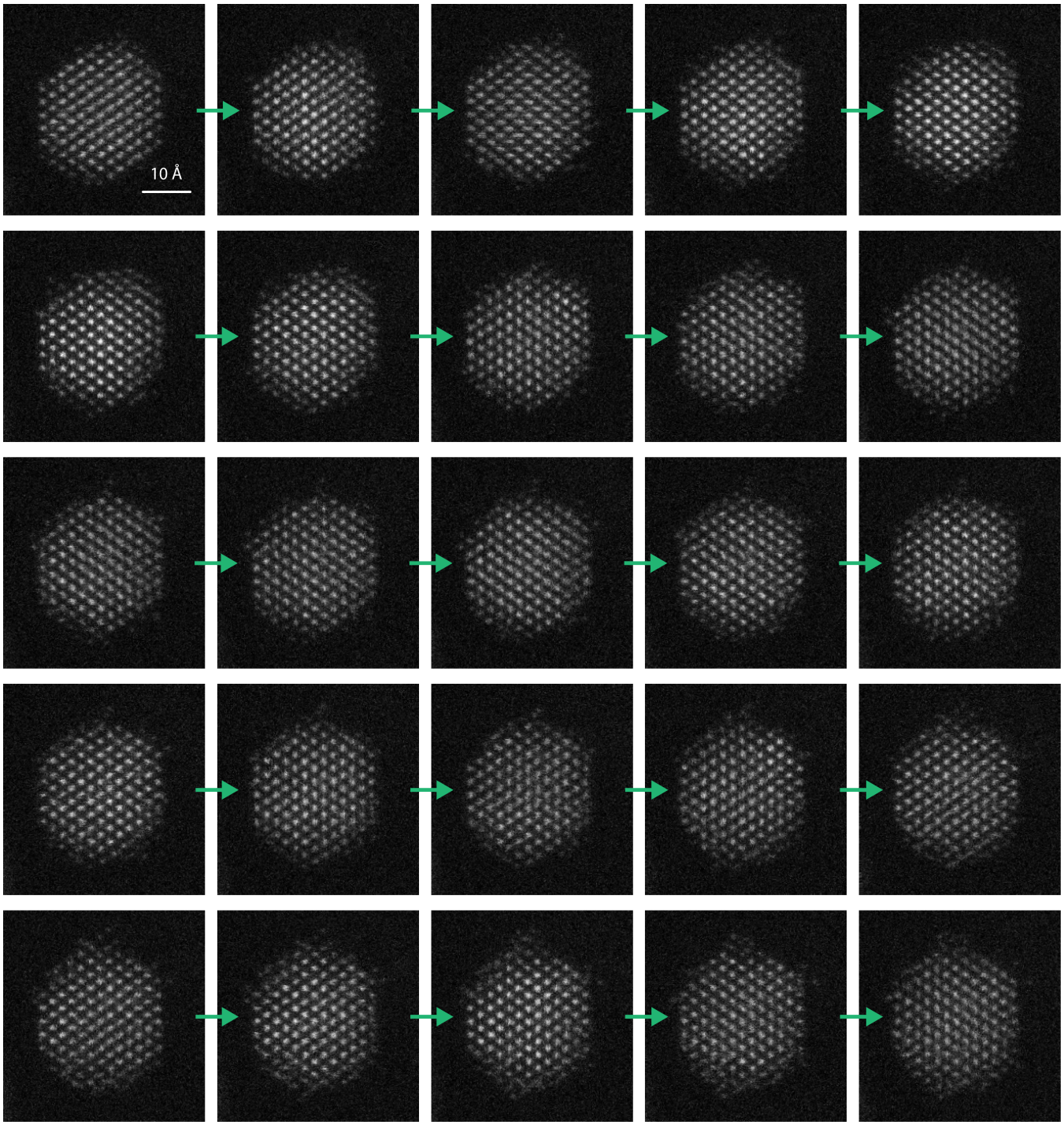

Figure 3. Experimental ADF STEM time-series of the Pt nanoparticle. Time progress along the rows.

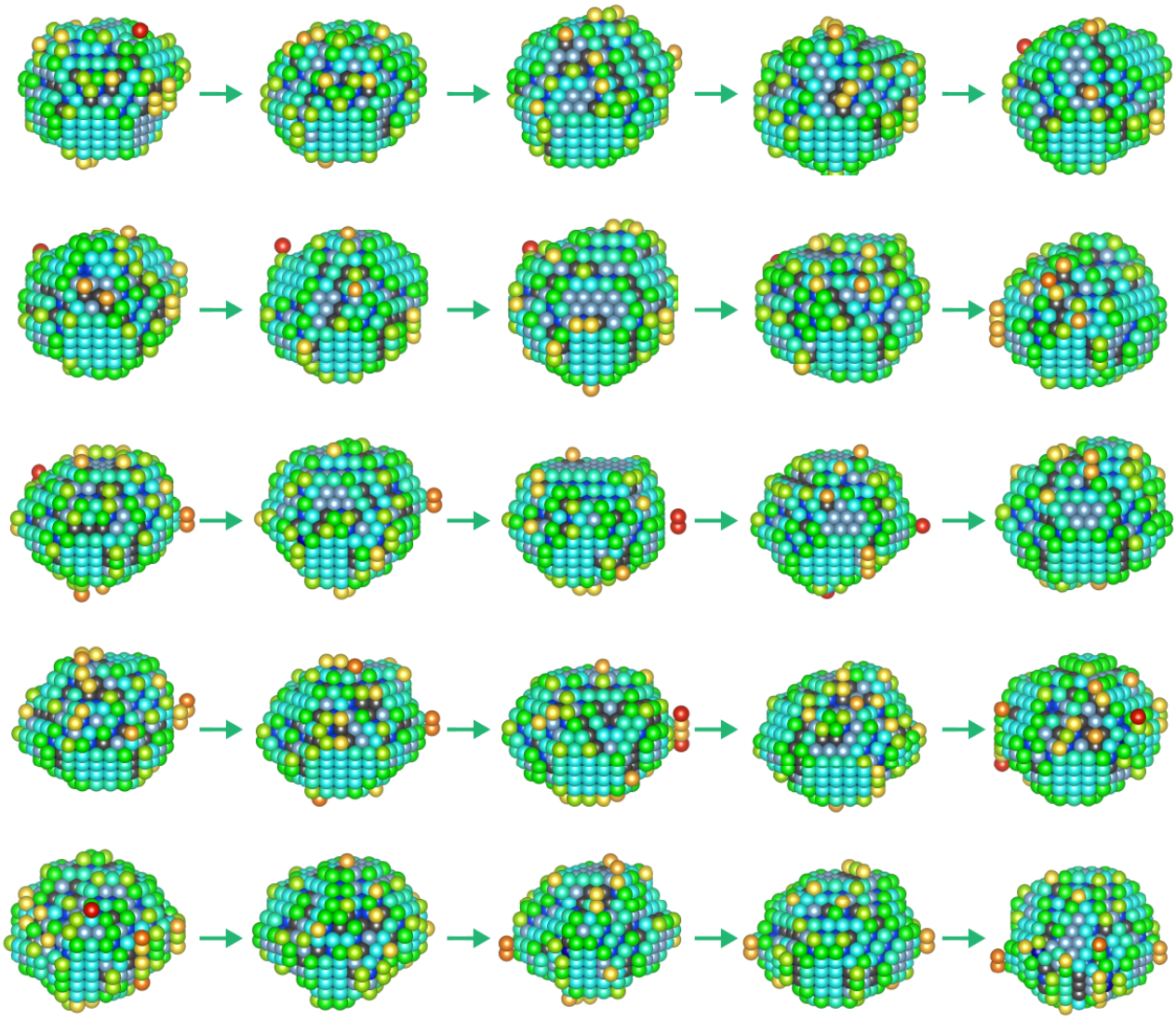

Figure 4. 3D atomic models obtained by the Bayesian genetic algorithm including the finite atom-counting precision and neighbor-mass relations as prior knowledge for the time series from Figure 2.

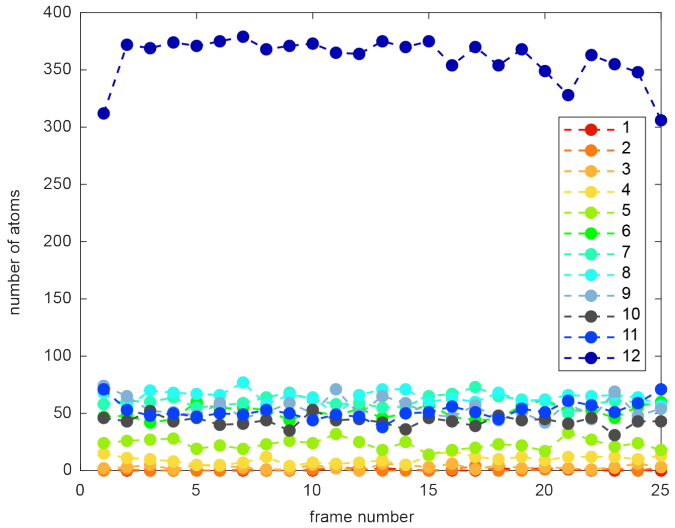

Figure 5. Atomic coordination number analysis for the time series of the Pt nanoparticle.